



Coupling thermoelectricity and electrocatalysis for hydrogen production via PbTe–PbS/TiO₂ heterojunction



Zhongqing Liu^{a,*}, Xiaohao Cao^a, Bin Wang^a, Min Xia^b, Sidney Lin^c, Zhanhu Guo^d, Xiaoming Zhang^a, Shiyuan Gao^a

^a School of Chemical Engineering, Sichuan University, Chengdu 610065, Sichuan, PR China

^b School of Materials Science and Engineering, University of Science and Technology Beijing, Beijing 100083, PR China

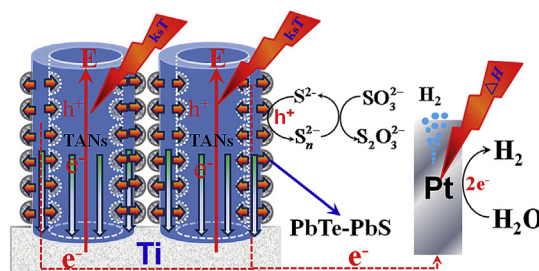
^c Dan F. Smith Department of Chemical Engineering, Lamar University, Beaumont, TX 77710, USA

^d Chemical and Biomolecular Engineering Department, University of Tennessee, Knoxville, TN 37996, USA

HIGHLIGHTS

- In situ cool side was proposed to address temperature non-equilibrium.
- Coupling thermoelectricity and electrocatalysis for hydrogen production.
- The energy of low quality heat sources is converted into chemical energy (H₂).
- The system registered an energy efficiency of 90%.
- The system consumed electric power less than about 40% of SPE method.

GRAPHICAL ABSTRACT



ARTICLE INFO

Article history:

Received 19 September 2016

Received in revised form

21 December 2016

Accepted 23 December 2016

Keywords:

PbTe–PbS

Thermoelectricity

Electrocatalysis

Hydrogen production

Heterojunction

ABSTRACT

PbTe–PbS/TiO₂ electrodes are produced via wet chemical routes for splitting water into hydrogen at the ambient temperatures. PbTe nano-crystals are firstly deposited via the successive ionic layer adsorption and reaction (SILAR) treatment onto TiO₂ nanotube arrays (TNAs) prepared by anodic oxidation of Ti substrates. Subsequently, linear sweep voltammetry (LSV) is employed to convert the outer PbTe into PbS, producing PbTe–PbS/TiO₂ electrodes with a gradient p–n–n band configuration. With the external electric field, the vector charge transfer effect of the TNAs and the gradient energy band structure of PbTe–PbS/TNAs, the two electrode system in which PbTe–PbS/TNAs functions as the anode illustrates excellent hydrogen production activities. The whole electrochemical system consisted of anode, cathode, electrolyte serves as a hot side while the endothermic electrochemical reactions in hydrogen production as an in situ cold side. At 70 °C and 1.0 V bath voltage, the system registers 6.1 mL cm^{−2} h^{−1} rate of hydrogen generation, consuming electric power of 26.2 kW h kg^{−1} H₂, with an energy efficiency of 88.5% and a heat efficiency of 49.9%. This method demonstrates a novel pathway to produce chemical energy from low quality waste heat, benefitting from thermoelectric and electrocatalytic coupling.

© 2016 Elsevier B.V. All rights reserved.

1. Introduction

There exists an urgent need worldwide for the development and utilization of new, clean energy sources replacing fossil fuels because of the issues associated with aggravated fossil fuel supply

* Corresponding author.

E-mail address: liuzq_hgxy@scu.edu.cn (Z. Liu).

crisis and greenhouse gas emissions. An attractive method to generate renewable energy is the hydrogen production via electrolysis of water [1]. Alkaline water electrolysis is one of the most feasible methods for hydrogen production, usually with a DC energy efficiency of 75% [2]. Solid polymer electrolyte (SPE) water electrolysis technology, first developed by General Electric in the 1960s for spacecraft applications, demonstrated significant advantages over conventional alkaline electrolyte water electrolysis [3]. The advantages of SPE include using a less corrosive electrolyte, having a higher volume specific hydrogen production capacity, and offering higher product purities and higher efficiencies in the range of 90–95%. However, there are several disadvantages of the SPE electrolysis. SPE electrolyzers have more special requirements on the components, including expensive polymer membranes and porous electrodes, and current collectors [4]. The thermodynamic voltage of water electrolysis is 1.23 V at 25 °C, corresponding to a theoretical electric consumption of 32.9 kW h kg⁻¹H₂. Because of the high overvoltage associated with the water hydrolysis process, the actual electric consumption is as high as 45–60 kW h kg⁻¹H₂. A critical problem facing both alkaline electrolysis and SPE is to lower the overvoltage in order to reduce electric consumption [2,3,5]. Noble metals (Pt, Pd, Ir, Ru, etc.) provide an excellent electrocatalytic surface that lowers the overvoltage, exemplified by an anodic electrocatalyst with the formula Ir_xRu_yTa_zO₂ having been claimed to achieve an overall voltage of 1.567 V at 1 A cm⁻² and 80 °C, equating to an electric consumption of 42 kW h kg⁻¹H₂ and an efficiency of 94% [6]. However, the scarce availability and high cost of precious metals limit their large, industry-scale applications. To gain the industry-scale application of hydrogen production, non-precious metal catalysts in combination with utilization of solar energy are strongly favored under the premise of both low materials cost and reduced energy input.

A recent research thrust acquiring enormous attention is the photocatalytic hydrogen production using TiO₂, derived from the famous photo irradiated water splitting research back in 1972 [7]. Over the past four decades, a vital scientific question encountered in this area is to enhance the visible light response of TiO₂ and to decrease the recombination of photo-induced charge carriers [8,9]. One very promising approach involves the sensitization of TiO₂ with narrow band gap quantum dots to address these issues [10]. A recent report employs a CdSe/TiO₂ heterojunction structure which demonstrates high photoelectrocatalytic hydrogen generation activities [11]. In the study, the authors deposited CdSe quantum dots (QDs) on both TiO₂ particulate and nanowire mesoporous structures to enable the wide band gap TiO₂ to absorb visible light. We have incorporated PbS QDs into highly ordered TiO₂ nanotube arrays (TNAs) by SILAR for photoelectrocatalytic hydrogen production [12]. The system demonstrated a peak photo conversion efficiency of 5.41%. However, the practical application of photocatalytic hydrogen production is limited by the low solar energy density and low energy conversion. Photocatalytic hydrogen production on large scales is still not optimized as compared to the existing SPE water electrolysis or alkaline water electrolysis.

One active research area based on exploring the similar semiconductor materials as the aforementioned QDs is thermoelectricity. In thermoelectric studies, the key is to improve the thermoelectric efficiency [13]. Lead chalcogenides such as PbTe have been intensively investigated in related studies. PbTe has a narrow band gap of 0.32 eV, a large Bohr exciton radius of 46 nm, a low thermal conductivity of 2.06 W m⁻¹ K⁻¹ (25 °C), a high electrical conductivity range of 28.29–99.50 S cm⁻¹ (25 °C), and high charge carrier (hole) transport rate of 1730 cm² V⁻¹ s⁻¹. These characteristics make PbTe among the most studied thermoelectric materials. Nanoscale inclusions within the host material have shown to significantly improve the thermoelectric properties.

Among the better-performing PbTe-based alloys, the PbTe–PbS system proves specifically interesting because these alloys can evolve into nanoscale heterogeneities that highly reduce thermal conductivity [14]. Epitaxial growth of PbS layer on PbTe nanoparticles produces PbTe–PbS core-shell composites that show very high electrical conductivity because of the doping-like effect as well as reduced thermal conductivity [15]. By manipulating the PbTe and PbTe–PbS structures via band engineering, band degeneracy, and phase separation, these materials have shown striking potentials for thermoelectric applications. Current studies in the field focus on materials suitable for the intermediate temperature range, i.e., 200–800 °C. There exists vast amounts of waste heat at <100 °C temperature range in many industries such as (nuclear) power generation, chemical manufactory, and metallurgy. Another low temperature energy source is hot water heated by sunlight. However, the efficiency of currently available thermoelectric materials at <100 °C is too low to convert the low quality waste heat sources into electricity at meaningfully large scales.

Here, we propose a novel system that may invoke the coupling of electrocatalytic water electrolysis and thermoelectric engineering [16]. This system consists of an anode, a cathode, and the electrolyte functioning as the hot side, while the endothermic electrochemical hydrogen production as the in situ cold side. This cold side is generated with the onset of the electrochemical reaction of hydrogen production, while it disappears simultaneously when hydrogen gas is released from the electrode surface. In the system, the sacrificial electrolyte of mixed Na₂S and Na₂SO₃ is consumed as the anodic half-cell reaction, S²⁻ + SO₃²⁻ → S₂O₃²⁻ + 2e⁻. Under the standard condition with both unbiased cathode and anode, the overall enthalpy change of the system, i.e., the cold side, is +173 kJ mol⁻¹H₂. With an applied electric field, the vector charge carrier transportation in the TiO₂ nanotube arrays and the gradient energy band structure of the PbTe–PbS/TNAs electrode converge to afford an enhanced performance. The convergence enormously augments the heat-excitation of electrons from donor energy level near Fermi level of (n)PbTe and holes from acceptor energy levels near Fermi level of (p)PbS. The transport and extraction of the heat-induced charge carriers are significantly accelerated within the PbTe–PbS/TNAs electrode. At 70 °C and 1.0 V bath voltage, the two electrode system with PbTe–PbS/TNAs as the anode registered an energy efficiency of 88.5% and a heat efficiency of 49.9%, consuming electric power of 26.2 kW h kg⁻¹H₂.

2. Experimental section

2.1. Materials synthesis

TiO₂ nanotube arrays (TNAs) were prepared via anodic oxidation, according to our previous work [12,17]. The prepared amorphous TNAs were treated at 500 °C in air for 2 h to transform to anatase TiO₂. The plugs of the nanotube openings were cleaned with 10 vol% H₂O₂ under ultrasonication. The TNAs were then immersed in 5 g L⁻¹ NaOH for 2 h and washed with water. The obtained TNAs were used as the support to deposit PbTe or PbS nano-crystals via SILAR method. 0.01 mol L⁻¹ Pb(Ac)₂ was used as the lead source, 0.1 mol L⁻¹ NaHTe containing 0.1 mol L⁻¹ NaBH₄ as the telluride source, and 0.1 mol L⁻¹ Na₂S as the sulfur source. One SILAR cycle consisted of Pb(Ac)₂ immersion, wash and drying, NaHTe/NaBH₄ or Na₂S immersion, wash and drying again. The deposition was carried out at 40 ± 1 °C, 30 min each immersion with N₂ agitation. The total SILAR cycles for both PbTe/TNAs and PbS/TNAs were five times. The freshly prepared PbTe/TNAs was used as the anode, Pt as the counter electrode, SCE as the reference electrode, and 0.5 mol L⁻¹ Na₂S solution was used as the electrolyte.

At 20 ± 1 °C, the surface of PbTe nano-crystals was converted into PbS via linear sweep voltammetry with potential scan range of -0.5 – 0.5 V, scanning rate of 0.01 V s^{-1} , and five repeats to produce PbTe–PbS/TNAs.

2.2. Characterization techniques

The samples were analyzed with X-ray diffraction (Philips XPert pro MPD) to afford the crystal phase composition, transmission electron microscopy (Tecnai G2 F20 S-Twin) to provide the micro morphology, and X-ray photoelectron spectroscopy (XSAM 800) with Ar ion stripping to produce chemical composition.

2.3. Electrochemical measurements

The J - V curves, Tafel plots and EIS measurements of the samples were conducted on an electrochemical work station (Shanghai Chenhua CHI650E) using a three-electrode quartz electrolytic cell, under magnetic stirring at 20 – 70 °C, 0.5 mol L^{-1} Na_2S and 0.5 mol L^{-1} Na_2SO_3 as the electrolyte, a potential scan range of -0.5 – 0.5 V, and a scan rate of 0.01 V s^{-1} . TNAs, PbS/TNAs, or PbTe–PbS/TNAs was used as the working electrode, Pt as the counter electrode, and saturated calomel electrode (SCE) as the reference electrode. The hydrogen production experiments were conducted at a direct current potentiostat in a two-electrode cell. TNAs, PbS/TNAs, or PbTe–PbS/TNAs was the anode and Pt the cathode, with an inter-electrode distance of 10 cm and fixed cell voltage of 1.0 V for 30 min. The other conditions were the same as the J - V test. The volume of produced H_2 gas was measured via water expulsion with a specifically scaled upside-down funnel.

3. Results and discussions

Fig. 1 depicts XRD patterns of the samples. In Fig. 1a, diffraction peaks of Ti substrate and anatase TiO_2 can be distinguished. After deposition of PbTe nano-crystals via the SILAR treatment, the (200), (220), (222), (400), (420), and (422) peaks of PbTe (JCPDS#65-0470) are displayed (Fig. 1b) [18,19]. It can be seen from Fig. 1c that compared to that of PbTe/TNAs, the strength of PbTe diffractions of the PbTe–PbS/TNAs sample is obviously reduced while new diffractions of (111), (200), (220) assigned to PbS phases (JCPDS#05-0692) are unveiled [19]. The reduced PbTe diffraction strength in PbTe–PbS/TNAs is attributed to the covering of PbTe surface by PbS. To form the epitaxial PbS onto PbTe nano-crystals, in situ substitution of sulfur for tellurium was introduced because of the lower

formation enthalpy of PbS (-98.74 kJ mol^{-1}) than that of PbTe (-69.50 kJ mol^{-1}) ($PbTe + S^{2-} \rightarrow PbS + Te^{2-}$). The in situ displacement of Te with S on PbTe nano-crystals is the combined effects of higher affinity between Pb and S than between Pb and Te, and the field induced diffusion of S^{2-} towards PbTe nano-crystals.

Electron microscopy images of PbTe/TNAs are shown in Figs. 2 and S1. There is a significant number of PbTe nano-crystals anchored onto the TiO_2 nanotubes. The profile inside the cross-section (Fig. S1a) shows the nano-crystals having an average diameter of 6 – 8 nm (Fig. S1b). The morphology of the PbTe nano-crystals appears ellipsoidal, with very good contact with the TiO_2 substrate (Fig. 2a). Fig. 2b illustrates the PbTe and TiO_2 regions that show the lattice spacings of 0.323 and 0.352 nm ascribed to the PbTe (200) (Fig. 2c) and TiO_2 (101) (Fig. 2d) facets, respectively [18,19]. Electron microscopy images of the resulting PbTe–PbS/TNAs are displayed in Figs. 3 and S2. From Fig. S2a, the composite nano-crystals deposited onto the TiO_2 nanotubes are clearly discernible. The number of nano-crystals of <4 nm diminishes, of 4 – 6 nm decreases, of 8 – 10 nm remains, of 10 – 14 nm increases, and the average diameter of the composite PbTe–PbS nano-crystals increases slightly to 7 – 9 nm (Fig. S2b). The bottom-up constructed interfaces between TiO_2 and PbTe and between PbTe and PbS can be distinguished in Fig. 3a, while the TiO_2 (101) spacing of 0.352 nm is revealed in Fig. 3b. From Fig. 3c, e and 3g, besides the PbTe (200) and TiO_2 (101) lattice planes, the crystal face with interstitial distance of 0.210 nm, corresponding to the PbS (220) facet, can be finely resolved [18]. Fig. 3d and f correspond to the Fourier transform diagrams of Fig. 3e and g, respectively. In addition, with increasing linear sweep voltammetry times, the circuit current density slightly dwindles in the potential range from -0.5 V to 0.5 V (Fig. S3), suggesting in situ formation of PbS at the PbTe nano-crystals surface.

X-ray photoelectron spectroscopy (XPS) was performed to demonstrate the chemical composition of PbTe/TNAs and PbTe–PbS/TNAs (Figs. S4 and S5), with the results tabulated in Table 1. In Fig. S4, the peak at 255.0 eV is assigned to the binding energy of S(2s), revealing the existence of S in PbTe–PbS/TNAs besides the other four elements. In PbTe/TNAs, the peak of Pb($4f_{5/2}$) at 137.6 eV can be attributed to Pb^{2+} in PbTe. The peak of Te($3d_{5/2}$) at 571.4 eV corresponds to Te^{2-} in PbTe. In PbTe–PbS/TNAs (Fig. S5), the binding energy of Pb($4f_{5/2}$) can be deconvoluted into peaks of 137.7 and 137.2 eV, corresponding to Pb in PbS and PbTe, respectively [16]. The peak of Te($3d_{5/2}$) at 571.7 eV can be ascribed to Te in PbTe [18–20]. According to Table S1, PbTe/TNAs renders a Te/Pb ratio of 1.07 relative to PbTe. In PbTe–PbS/TNAs, the ratio is reduced drastically to 0.25 . It indicates that the resulting composite PbTe–PbS nano-crystals possess n-type PbTe cores after linear sweep voltammetry [21]. In the meantime, the S/Pb ratio is 2.17 relative to PbS, representing the in situ formation of p-type PbS at outer PbTe [22]. No evidence of alloying, oxidation, or the presence of a $PbTe_xS_{1-x}$ interface layer could be obtained by either HRTEM or XRD. Accordingly, the in situ formed PbS at the PbTe QD surface is proposed, and a p-n-n band configuration from PbS to PbTe and then TiO_2 is constructed. The band gaps (E_R) of the nanoscale semiconductor materials were calculated using Brus formula [23]:

$$E_r = E_g + \frac{h^2}{8r^2} \left(\frac{1}{m_e^*} + \frac{1}{m_h^*} \right) - \frac{1.8e^2}{4\pi\epsilon_0\epsilon_r r} \quad (1)$$

where r is the radius, here defined as mean radius of PbTe or PbS nano-crystals; m_e^* and m_h^* are effective masses of electrons and holes, respectively; ϵ_0 and ϵ_r are the vacuum permittivity and the relative permittivity of nano-crystals material, respectively; h and e

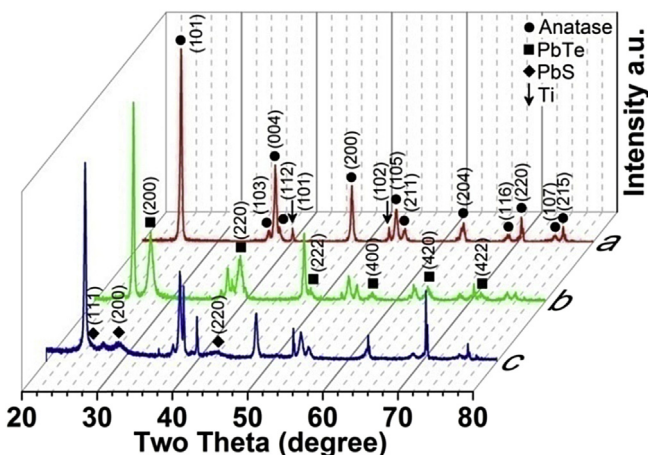


Fig. 1. XRD patterns of (a) TNAs, (b) PbTe/TNAs and (c) PbTe–PbS/TNAs.

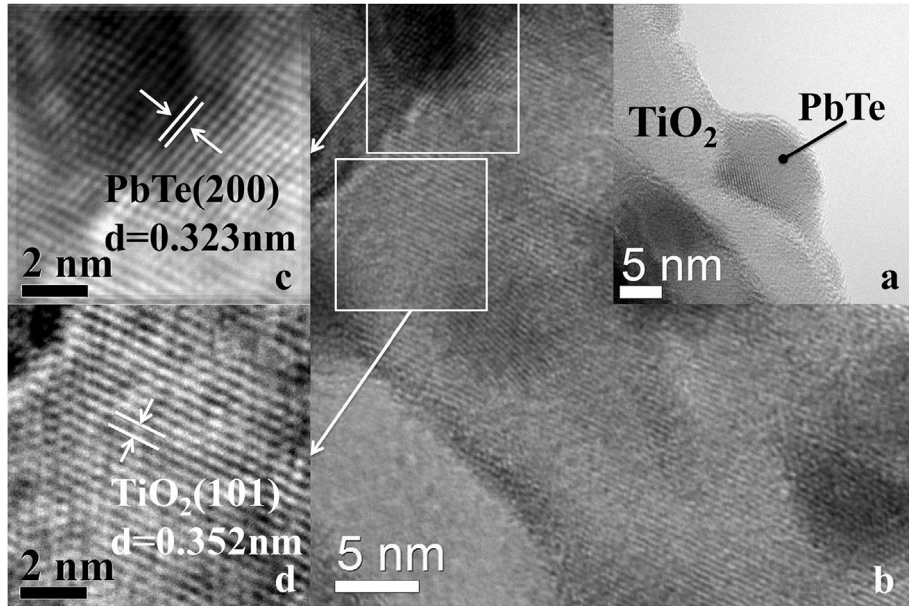


Fig. 2. (a) TEM image of a single PbTe nano-crystal and TiO₂ substrate. (b) TEM image of PbTe/TNAs. (c) HRTEM image labeled by a square in (b) for PbTe (200) facet. (d) HRTEM image labeled by a square in (b) for TiO₂ (101) facet.

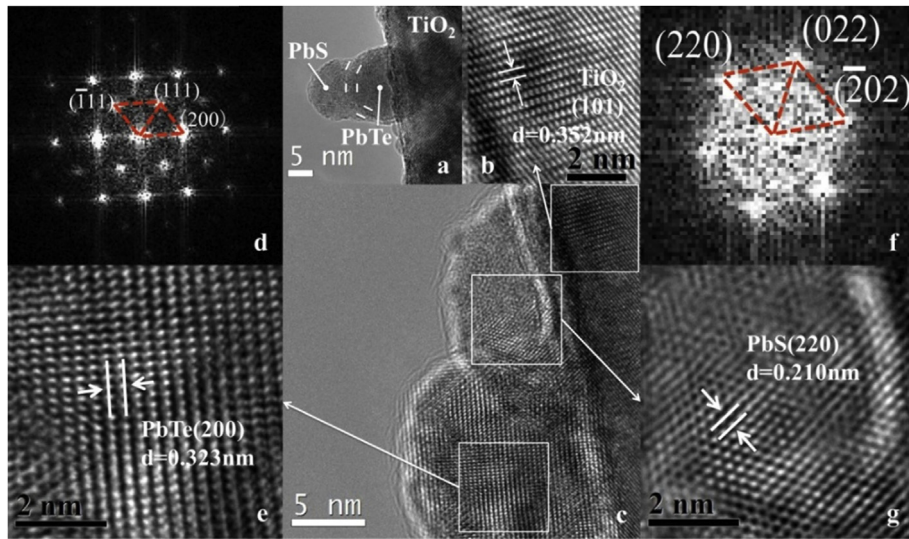


Fig. 3. (a) TEM image of composite PbTe–PbS nano-crystal and TiO₂ substrate. (b) HRTEM image labeled by a square in (c) for TiO₂ (101) facet. (c) TEM image of PbTe–PbS/TNAs. (d) Fourier transform (FFT) diagram corresponding to (e). (e) HRTEM image labeled by a square in (c) for PbTe (200) facet. (f) FFT diagram corresponding to (g). (g) HRTEM image labeled by a square in (c) for PbS (220) facet.

Table 1
Chemical composition of the samples (Atomic%).

Sample	O O		Ti	Te			Pb			S
	Chemisorbed O ₂	TiO ₂	TiO ₂	TeO ₂	Na ₂ Te	PbTe	PbS	PbTe	Pb	PbS
PbTe/TNAs	44.25	30.91	9.28	3.22	–	4.82	–	4.50	3.02	–
PbTe–PbS/TNAs	35.65	25.48	9.61	1.01	0.69	1.35	6.59	5.35	–	14.27

are the Planck constant and basic charge, respectively; and E_g is the band gap of the bulk material. According to the calculation, the band gaps of PbTe and PbS are 1.19 eV and 0.93 eV for PbTe–PbS nano-crystals, respectively. The conduction band levels were estimated by using the formula:

$$E_{CB} = X - 4.5 - 0.5E_r \tag{2}$$

where X is the absolute electronegativity of the semiconductor, expressed as the geometric mean of the Sanderson

electronegativity of the constituent atoms. The calculated conduction band levels are -3.384 eV, -2.853 eV and -2.582 eV for TiO_2 , PbTe and PbS , respectively. Thus the conduction position of PbS is 0.271 eV higher than that of PbTe , while that of PbTe is 0.531 eV higher than that of TiO_2 . The electrons are located in PbTe nano-crystals, and holes in PbS nano-crystals, respectively. It is expected that high density of positively charged sites is induced at the PbS nano-crystals. This polarization configuration of charge carries can significantly promote anodic reaction, and accelerate transfer of charge carries in PbTe-PbS/TNAs [15].

The $J-V$ curves of TNAs, PbS/TNAs and PbTe-PbS/TNAs at various temperatures are shown in Fig. 4, while the short circuit current densities of the samples are tabulated in Table S1. During electrochemical experiments, the use of $\text{Na}_2\text{S}/\text{Na}_2\text{SO}_3$ electrolyte pair presented a high S^{2-} ion concentration in the solution. The S^{2-} ions replaced the outer layer of PbTe to form PbS . Therefore PbTe/TNAs were converted to PbTe-PbS/TNAs , and the data recorded were for PbTe-PbS/TNAs , rather than for PbTe/TNAs . From the $J-V$ curves, the temperature-dependent electrochemical responses of the samples follow this order: $\text{TNAs} \ll \text{PbS/TNAs} \ll \text{PbTe-PbS/TNAs}$. Among the samples, TNAs showed the lowest electrochemical response with a short circuit current density of 0.61 mA cm^{-2} at 70°C . The values of PbS/TNAs is 5.30 mA cm^{-2} , 8.7 times that of the TNAs. PbTe-PbS/TNAs exhibited the highest electrochemical response with increasing temperature, presenting a short circuit current density of 44.03 mA cm^{-2} at 20°C (Table S2), 19.14 times that of CdSe/TiO_2 heterojunction (2.3 mA cm^{-2}) [11], and reaching $193.80 \text{ mA cm}^{-2}$ at 70°C , 36.6 times that of the PbS/TNAs . Note that $J-V$ plots of the PbTe-PbS/TNAs appear similar to that of a metal thin film in the whole potential scan range.

The $J-V$ experiment results demonstrate that PbTe-PbS/TNAs possessed the highest electrochemical response, suggesting this electrode could afford excellent hydrogen production [12]. With a bath voltage of 1.0 V , aqueous solution of $0.5 \text{ mol L}^{-1} \text{ Na}_2\text{S}$ and 0.5

$\text{Na}_2\text{SO}_3 \text{ mol L}^{-1}$ as the sacrificial electrolyte, the hydrogen production experiments were performed using a two-electrode system in the temperature range of $20\text{--}70^\circ\text{C}$. TNAs, PbS/TNAs , or PbTe-PbS/TNAs functioned as the anode, and Pt as the cathode. The hydrogen generation rates, Faraday efficiencies, and electricity consumption of the samples are given in Fig. 5 (See Methods in supplementary materials). In Fig. 5a, PbTe-PbS/TNAs boasts very high hydrogen generation rates while TNAs has negligible activity and not continued in the ensuing experiments. At 20°C , the hydrogen production rate of PbTe-PbS/TNAs reached $2.4 \text{ mL cm}^{-2} \text{ h}^{-1}$, 35.8 times that of PbS/TNAs ($0.067 \text{ mL cm}^{-2} \text{ h}^{-1}$). At 70°C , the value of PbTe-PbS/TNAs increased to $6.1 \text{ mL cm}^{-2} \text{ h}^{-1}$, 14.5 times that of PbS/TNAs ($0.42 \text{ mL cm}^{-2} \text{ h}^{-1}$). Fig. 5b reveals the Faraday efficiency of PbS/TNAs decreases with increasing temperature, registered the maximum of 49.6% at 20°C . Conversely, the Faraday efficiency of PbTe-PbS/TNAs increases with increasing temperature, the value arrived 80.29% at 20°C , already achieved 99.9% of that at 50°C . The consumed electric energy of hydrogen production arrived the minimum of $54.5 \text{ kW h kg}^{-1}\text{H}_2$ at 20°C for PbS/TNAs and rapidly increased with increasing temperature. On the contrary, the consumed electric energy of PbTe-PbS/TNAs slightly decreased with temperature increment, and was $26.2 \text{ kW h kg}^{-1}\text{H}_2$ at 70°C , about 40% lower than that registered by conventional SPE water electrolysis or alkaline water electrolysis [2,6]. The hydrogen production experiments strongly verify the outstanding electrocatalytic activity of PbTe-PbS/TNAs .

Fig. 6a displays the Tafel plots of samples. The TNAs and PbS/TNAs possess Tafel slopes of 172 and 192 mV dec^{-1} , respectively, and close to the exchange current densities within the 10^{-3} range. The exchange current density of PbTe-PbS/TNAs is $5.07 \times 10^{-2} \text{ mA cm}^{-2}$ and one order of magnitude higher than that of TNAs and PbS/TNAs , with significantly reduced Tafel slope of 95 mV dec^{-1} , suggesting much better reversibility and higher electrode activity [24]. Fig. 6b illustrates the electrochemical

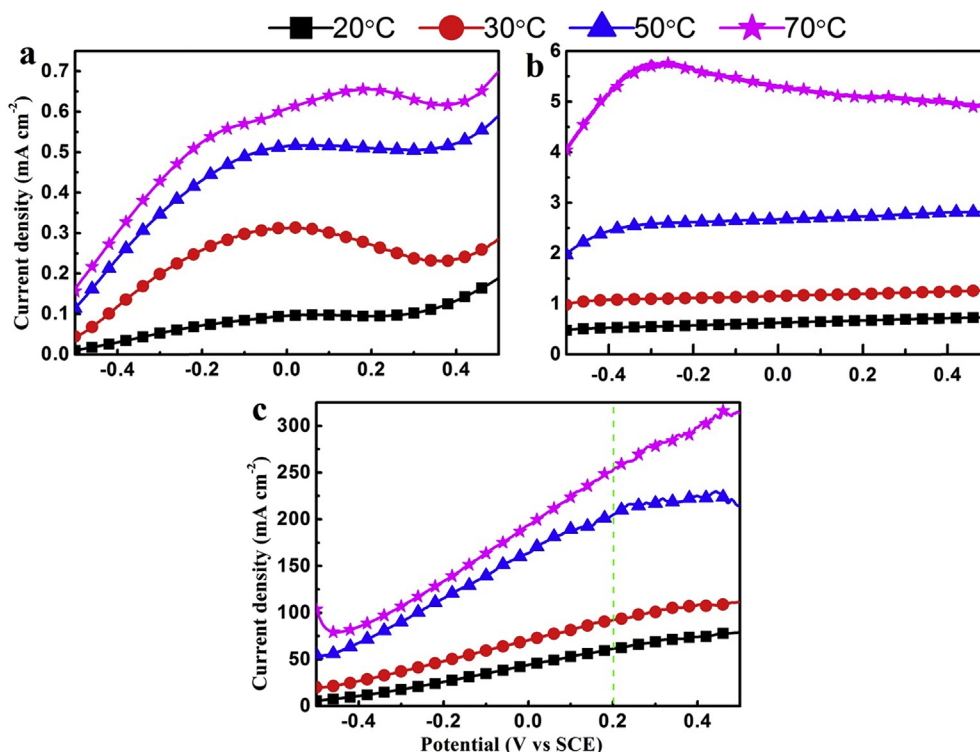


Fig. 4. $J-V$ curves of (a) pristine TNAs, (b) PbS/TNAs and (c) PbTe-PbS/TNAs at various temperatures for three electrodes system.

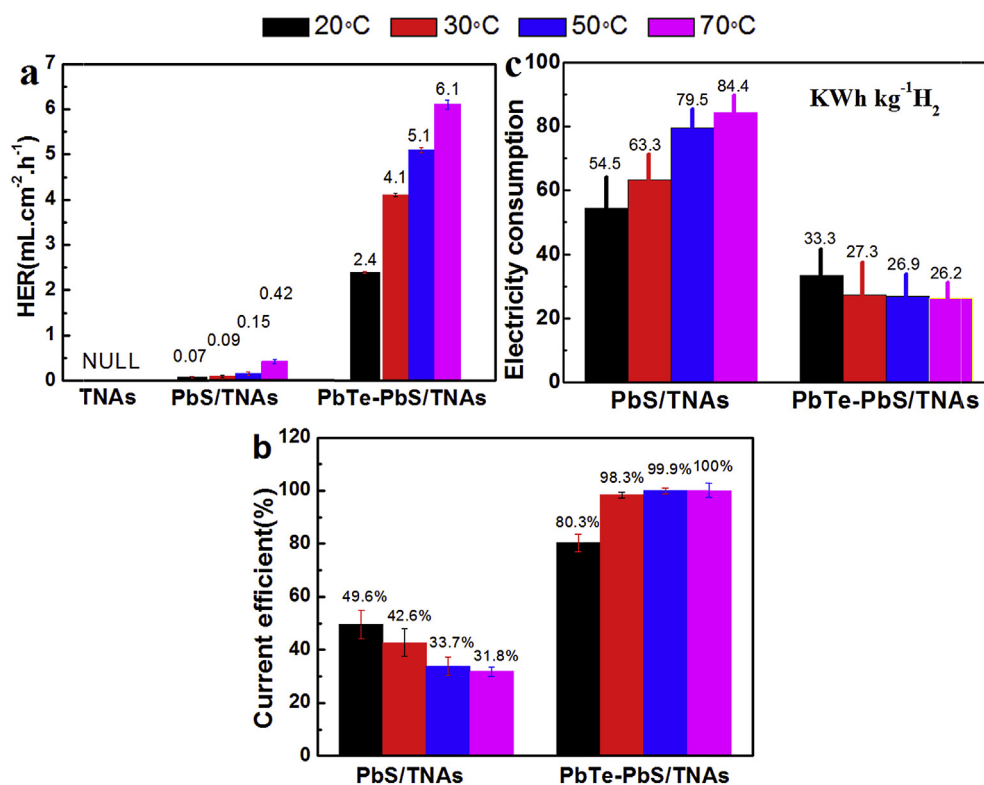


Fig. 5. Hydrogen generation rates (a), current efficiencies of hydrogen generation (b), and electrical energy consumption of hydrogen generation (c) of the samples at various temperatures.

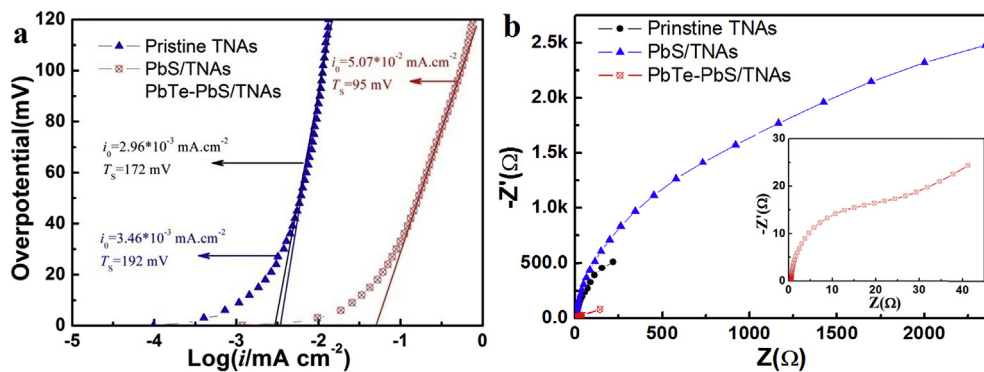


Fig. 6. (a) Tafel curves and (b) EIS plots of the samples at 20 °C. The inset in (b) is the enlarged EIS plot of the PbTe-PbS/TNAs.

impedance spectroscopy (EIS) curves of the samples. The radii of the low frequency arc portion represent the magnitude of electrode reaction resistances [25]. By employing the simulated equivalent circuit [12], the electrochemical reaction resistance of PbTe-PbS/TNAs was calculated to be 11.5 Ω cm⁻², only 0.24% of that of TNAs (4705.9 Ω cm⁻²) and 0.28% of that of PbS/TNAs (4065.2 Ω cm⁻²). It can be deduced after introduction of PbTe-PbS nano-crystals, that the charge carrier concentration is increased significantly which in turn enhanced conductivity and hot charge carrier extraction of the PbTe-PbS/TNAs electrode [15,18,26].

In Fig. 7a, the external circuit anodic current densities of the two-electrode hydrogen production electrolysis system using PbTe-PbS/TNAs as the anode are shown in the temperature range of 20–70 °C. It can be seen that the current densities increased with increasing electrolyte temperature, indicating expedited electrochemical reaction rates of the electrolysis system versus

temperature [2]. The activation energies of the overall electrochemical reaction at various temperature calculated according to the Vant Hoff equation are demonstrated in Fig. 7b. The activation energies declined with increasing temperature. In the temperature range of 20–30 °C, the activation energy was 22.1 kJ mol⁻¹, suggesting that the overall reaction rate was controlled by both electrochemical reaction and diffusion. In the temperature range of 30–70 °C, the activation energies were 10.7, 3.0, 5.2, and 3.2 kJ mol⁻¹, respectively. It can be deduced that the electrochemical reaction rate was highly accelerated while the diffusion became the rate limiting step. The enthalpy of the overall electrochemical reaction slightly increased with increasing temperature and was about 183.6, 188.0, 192.7, and 208.4 kJ mol⁻¹ at 20 °C, 30 °C, 50 °C and 70 °C, respectively. Fig. 7c illustrated the column graphs of energy and heat efficiencies of the two-electrode system with PbTe-PbS/TNAs as the anode at different temperatures (See

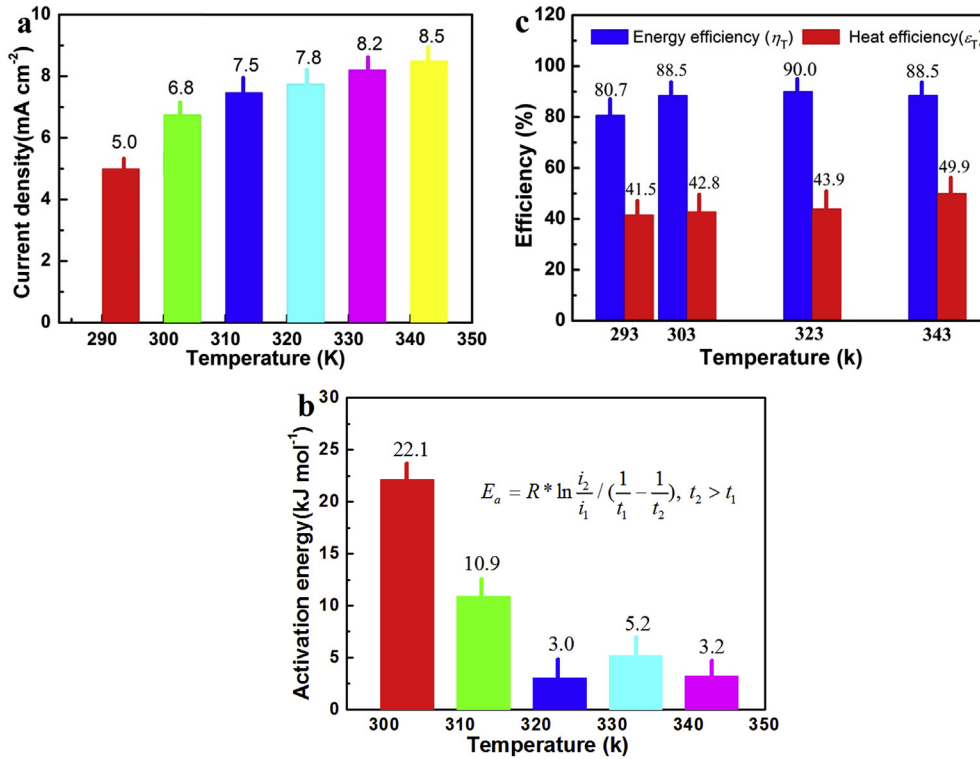


Fig. 7. Current density (a), activation energy (b), and energy and heat efficiencies (c) vs temperatures under 1.0 V bath voltage for the two electrodes system of PbTe–PbS/TNAs functioned as an anode.

Calculation Methods in [supplementary materials](#)). Within the experimental temperature range, energy efficiency reached the highest of 90% at 50 °C, which is comparable to conventional alkaline water electrolysis or SPE method, but without the use of noble metal catalyst [2,6]. In the meantime, heat efficiency rose with increasing temperature, reaching the highest of 49.9% at 70 °C. The hydrogen production rates at 20, 30, 50, and 70 °C, respectively, were used to calculate the high heating values of produced hydrogen gas per unit electrode surface area and time to be 30.41, 51.95, 64.62, and 77.28 J cm⁻² h⁻¹, respectively. The input electric energies at these individual temperatures were 18.0, 24.3, 27.9, and 30.6 J cm⁻² h⁻¹, respectively. The produced hydrogen gas energies were 1.69, 2.14, 2.31, and 2.53 times, respectively, of the input electric energies within the temperature range of 20–70 °C. According to thermodynamics, the chemical energy in hydrogen gas generated by water electrolysis comes from electricity and heat. The extra portion of energy in chemical energy form should be attributed to heat absorbed from the environment.

Combining the XRD, TEM, XPS and electrochemical results, we depict the relevant processes at the PbTe–PbS/TNAs anode of the thermoelectrochemical cell leading to the high efficient hydrogen production [27,28], shown in Fig. 8. For a certain semiconductor electrode, the generation and diffusion rates of free carriers are constant, and are closely related to the carrier density which controls the electrochemical reaction rate. Within the experimental temperature range of 20–70 °C, the thermal energy ($k_B T = 0.024\text{--}0.031$ eV) is too low to excite charge carriers with band gap excitation mode in the PbTe–PbS/TNAs system. The sources of free charge carriers in PbTe–PbS/TNAs electrode should be ascribed to the heat-induced conduction band electrons of the n-type PbTe from its donor energy levels, and the heat-excited valence band holes of the p-type PbS from its acceptor energy levels (Fig. 8b). At the interface of PbS and electrolyte, SO_3^{2-} and S^{2-} ions capture the heat-induced holes in PbS valence band ($\text{SO}_3^{2-} + \text{S}^{2-} + 2\text{h}^+ \rightarrow \text{S}_2\text{O}_3^{2-}$) [10,29]. The electrons transport axially to Ti substrate along the TiO₂ nanotubes, and arrive at the Pt

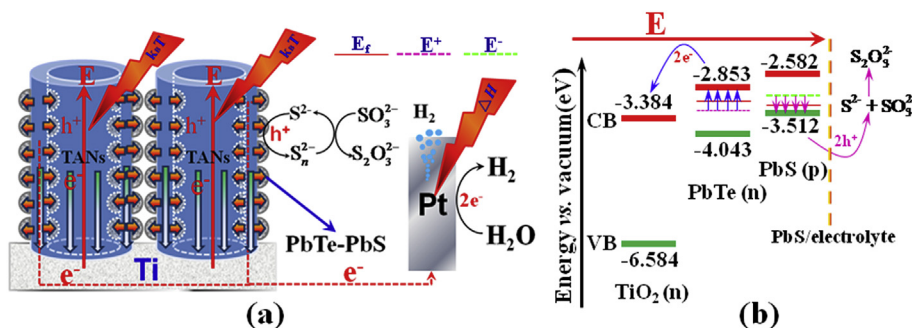


Fig. 8. (a) Proposed schematic diagram of the relevant processes leading to high efficiency hydrogen production via PbTe–PbS/TiO₂ heterojunction. (b) Energy level diagram of the PbTe–PbS/TNAs. E expresses applied electric field. E_f, E⁻, E⁺ denotes Fermi, acceptor and donor energy levels, respectively.

electrode via the external circuit to reduce water into hydrogen gas ($2\text{H}_2\text{O} + 2\text{e}^- \rightarrow 2\text{OH}^- + \text{H}_2$) [30]. With the electric field, chemical potential gradients, and vector charge transfer of TiO_2 nanotube, electrons are prompted to transport along the TiO_2 nanotube walls vertical to Ti substrate, whereas holes transport perpendicularly to the TiO_2 nanotube walls to the PbS layer. Under the situation, the whole electrochemical system acts as the hot side, while the endothermic electrochemical hydrogen production is the in situ cold side. The applied field assists to pump the heated-induced electrons toward the Pt electrode to reduce water via the external circuit, and the heated-induced holes toward the interface of PbS/electrolyte and are captured by SO_3^{2-} and/or S^{2-} ions. The reverse transport of the electrons or holes is blocked by the barriers of the PbTe–PbS/TNAs gradient band. With the coupling of the thermal excitation of charge carriers and the electrocatalytic process, the heat energy is converted into chemical energy (H_2) by the hydrogen evolution reaction assisted by electric field. The converging effect significantly facilitates transport and extraction of the heat-induced charge carriers together with electrochemical reactions.

4. Conclusions

In summary, we prepared PbS/TNAs and PbTe/TNAs via the SILAR method, using anodic oxidation produced TiO_2 nanotube arrays as the support. The PbTe/TNAs samples were subsequently used as the anode to undergo linear sweep voltammetry to produce PbTe–PbS/TNAs. PbS was in situ formed at the PbTe surface with a PbTe(n)–PbS(p) structure. During the water electrolysis process, the whole electrolysis system using PbTe–PbS/TNAs as the anode acted as the hot side, while the endothermic electrochemical reaction was the in situ cold side. At 70°C and 1.0 V cell voltage, the system recorded a $6.1\text{ mL cm}^{-2}\text{ h}^{-1}$ rate and 100% Faraday efficiency of hydrogen production, consuming electric power of 26.2 kWh kg^{-1}H_2 , with an energy efficiency of 88.5% and a heat efficiency of 49.9%. Under the applied electric field, chemical potential gradients, and vector charge transport in TiO_2 nanotube arrays, the processes of charge carrier heat-excitation and transport were significantly strengthened, accordingly presenting excellent hydrogen production activities.

Acknowledgements

This work was supported by the National Science Foundation of China (Grant no. 50774053 and 21376154). The authors would like to express their heartfelt gratitude to Analytical and Test Center of Sichuan University.

Appendix A. Supplementary material

Supplementary material related to this article can be found at <http://dx.doi.org/10.1016/j.jpowsour.2016.12.088>.

References

- [1] M. Wang, Z. Wang, X. Gong, Z. Guo, The intensification technologies to water electrolysis for hydrogen production – a review, *Renew. Sust. Energy Rev.* 29 (2014) 573–588.
- [2] K. Zeng, D. Zhang, Recent progress in alkaline water electrolysis for hydrogen production and application applications, *Prog. Energ. Combust. Sci.* 36 (2010) 307–326.
- [3] H. Cheng, K. Scott, P.A. Christensen, Paired electrolysis in a solid polymer electrolyte reactor- simultaneous reduction of nitrate and oxidation of ammonia, *Christ. Chem. Eng. J.* 108 (2005) 257–268.
- [4] F. Barbir, PEM electrolysis for production of hydrogen from renewable energy sources, *Sol. Energy* 78 (2005) 661–669.
- [5] J. Deng, P.J. Ren, D.H. Deng, L. Yu, F. Yang, X.H. Bao, Highly active and durable non-precious-metal catalysts encapsulated in carbon nanotubes for hydrogen evolution reaction, *Energy Environ. Sci.* 7 (2014) 1919–1923.
- [6] A.T. Marshall, S. Sunde, M. Tsyppkin, R. Tunold, Performance of a PEM water electrolysis cell using $\text{Ir}_x\text{Ru}_y\text{Ta}_z\text{O}_2$ electrocatalysts for the oxygen evolution electrode, *Int. J. Hydrogen Energy* 32 (2007) 2320–2324.
- [7] A. Fujishima, K. Honda, Electrochemical photolysis of water at a semiconductor electrode, *Nature* 238 (1972) 37–38.
- [8] G. Liu, H.G. Yang, J. Pan, Y.Q. Yang, G.Q. Lu, H.M. Cheng, Titanium dioxide crystals with tailored facets, *Chem. Rev.* 114 (2014) 9559–9612.
- [9] Q.P. Lu, Y.F. Yu, Q.L. Ma, B. Chen, H. Zhang, Two-dimensional transition metal dichalcogenide nanosheet-based composites for photocatalytic and electrocatalytic hydrogen evolution reactions, *Adv. Mater.* 28 (2016) 1917–1933.
- [10] J. Bai, J. Li, Y. Liu, B. Zhou, W. Cai, New glass substrate photoelectrocatalytic electrode for efficient visible-light hydrogen production: CdS sensitized TiO_2 nanotube arrays, *Appl. Catal. B* 95 (2010) 408–413.
- [11] P. Rodenas, T. Song, P. Sudhagar, G. Marzari, H. Han, L. Badia-Bou, S. Gimenez, F. Fabregat-Santiago, I. Mora-Sero, J. Bisquert, U. Paik, Y.S. Kang, Quantum dot based hetero structures for unassisted photoelectro- chemical hydrogen generation, *Adv. Energy Mater.* 3 (2013) 176–182.
- [12] Z.Q. Liu, B. Wang, J.C. Wu, Q. Dong, X.M. Zhang, H. Xu, Effects of hydroxylation on PbS quantum dot sensitized TiO_2 nanotube array photoelectrodes, *Electrochim. Acta* 187 (2016) 480–487.
- [13] Z.H. Dughaihs, Lead telluride as a thermoelectric material for thermoelectric power generation, *Phys. B Condens. Mater.* 322 (2002) 205–223.
- [14] J.R. Sootsman, D.Y. Chung, M.G. Kanatzidis, New and old concepts in thermoelectric materials, *Angew. Chem. Int. Ed.* 48 (2009) 8616–8639.
- [15] M. Ibáñez, R. Zamani, S. Gorsse, J. Fan, S. Ortega, D. Cadavid, J.R. Morante, J. Arbiol, A. Cabot, Core-shell nanoparticles as building blocks for the bottom-up production of functional nanocomposites: PbTe–PbS thermoelectric properties, *ACS Nano* 7 (2013) 2573–2586.
- [16] T.M. Tritt, H. Böttner, L.D. Chen, Thermoelectrics: direct solar thermal energy conversion, *Mrs Bull.* 33 (2008) 366–368.
- [17] X. Liu, Z.Q. Liu, J.L. Lu, X.L. Wu, B. Xu, W. Chu, Silver sulfide nanoparticles sensitized titanium dioxide nanotube arrays by in situ sulfurization for photocatalytic hydrogen production, *J. Colloid Interf. Sci.* 413 (2014) 17–23.
- [18] R. Jin, G. Chen, J. Pei, C. Yan, Hydrothermal synthesis and thermoelectric transport property of PbS–PbTe core–shell heterostructures, *New J. Chem.* 36 (2012) 2574–2579.
- [19] J.E. Murphy, M.C. Beard, A.G. Norman, S.P. Ahrenkiel, J.C. Johnson, P. Yu, O.I. Micic, R.J. Ellingson, A.J. Nozik, PbTe colloidal nanocrystals: synthesis, characterization, and multiple exciton generation, *J. Am. Chem. Soc.* 128 (2006) 3241–3247.
- [20] T.J. Zhu, X. Chen, Y.Q. Cao, X.B. Zhao, Controllable synthesis and shape evolution of PbTe three- dimensional hierarchical superstructures via an alkaline hydrothermal method, *J. Phys. Chem. C* 113 (2009) 8085–8591.
- [21] R.P. Bhatta, M. Henderson, A. Eufrazio, I.L. Pegg, B.J. Dutta, Properties of p- and n-type PbTe microwires for thermoelectric devices, *Electro. Mater.* 43 (2014) 4056–4063.
- [22] A.S. Obaid, M.A. Mahdi, Z. Hassan, M. Bououdina, PbS nanocrystal solar cells fabricated using microwave-assisted chemical bath deposition, *Int. J. Hydrogen Energy* 36 (2013) 807–815.
- [23] L.E. Brus, Electron–electron and electron–hole interactions in small semiconductor crystallites: the size dependence of the lowest excited electronic state, *J. Chem. Phys.* 80 (1984) 4403–4409.
- [24] Y. Li, H. Wang, L. Xie, Y. Liang, G. Hong, H. Dai, MoS_2 nanoparticles grown on graphene: an advanced catalyst for the hydrogen evolution reaction, *J. Am. Chem. Soc.* 133 (2011) 7296–7299.
- [25] Y. Yu, S.Y. Huang, Y. Li, S.N. Steinmann, W. Yang, L. Cao, Layer-dependent electrocatalysis of MoS_2 for hydrogen evolution, *Nano Lett.* 14 (2014) 553–558.
- [26] G.J. Snyder, E.S. Toberer, Complex thermoelectric materials, *Nat. Mater.* 7 (2008) 105–114.
- [27] J. Hensel, G.M. Wang, Y. Li, J.Z. Zhang, Synergistic effect of CdSe quantum dot sensitization and nitrogen doping of TiO_2 nanostructures for photoelectrochemical solar hydrogen generation, *Nano Lett.* 10 (2010) 478–483.
- [28] H.M. Chen, C.K. Chen, Y.C. Chang, C.W. Tsai, R.S. Liu, S.F. Hu, W.S. Chang, K.H. Chen, Quantum dot monolayer sensitized ZnO nanowire-array photoelectrodes: true efficiency for water splitting, *Angew. Chem. Int. Ed.* 49 (2010) 5966–5969.
- [29] N. Guijarro, Q. Shen, S. Gimenez, I. Mora-Sero, J. Bisquert, T. Lana-Villarreal, T. Toyoda, R. Gomez, Direct correlation between ultrafast injection and photoanode performance in quantum dot sensitized solar cells, *J. Phys. Chem. C* 114 (2010) 22352–22360.
- [30] M.A. Holmes, T.K. Townsend, F.E. Osterloh, Quantum confinement controlled photocatalytic water splitting by suspended CdSe nanocrystals, *Chem. Commun.* 48 (2012) 371–373.